Lab on a Chip

ROYAL SOCIETY OF CHEMISTRY

PAPER

View Article Online
View Journal

Check for updates

Cite this: DOI: 10.1039/d6lc00216a

Development of a 16-channel solid-state nanopore array platform for integrated nanopore fabrication and ionic current measurement

Itaru Yanagi, *[a] Tadashi Kiyuna,*[b] Keiko Esashika,*[c] Yoshimitsu Yanagawa,*[d] Hai Huy Nguyen Pham,*[d] Daiki Kawai,*[a] Satoshi Ogihara,*[a] Gaku Ogino,*[a] Ken-ichi Takeda*[d] and Sotaro Uemura *[a]

Parallel solid-state nanopore measurements are expected to improve not only throughput but also molecular discrimination performance. Here, we report the development of a 16-channel solid-state nanopore array measurement system that enables parallel nanopore fabrication by dielectric breakdown and subsequent ionic current recording. The system supports two fabrication modes: pulsed-voltage-induced dielectric breakdown (MPVI) and controlled dielectric breakdown (CBD) under constant-voltage bias, allowing nanopore formation over a wide diameter range. To demonstrate the operation of the developed system, two experimental studies were conducted. In the first study, nanopores were fabricated in 5 nm-thick SiN membranes using MPVI, followed by detection of single-stranded DNA (ssDNA) translocation. Arrays of nanopores with diameters ranging from 1 to 2 nm were formed, and the pore-diameter dependence of dwell time and current blockade amplitude during ssDNA translocation could be evaluated at sub-nanometer resolution. In the second study, nanopores were fabricated in 14 nm-thick SiN membranes using CBD, and double-stranded DNA (dsDNA) translocation was detected. Analysis of current traces during CBD suggested that pore enlargement remained limited for a period after dielectric breakdown, followed by accelerated pore growth accompanied by a rapid increase in current. The resulting pore diameters were distributed within 8–10 nm for 13 of the 16 channels and within 8–9 nm for 12 channels, demonstrating tight size control across most channels. Using these fabricated nanopores, dsDNA translocation events were observed in all channels.

Received 7th March 2026,
Accepted 23rd April 2026

DOI: 10.1039/d6lc00216a

rsc.li/loc

Open Access Article. Published on 06 May 2026. Downloaded on 5/27/2026 1:15:12 PM.
This article is licensed under a Creative Commons Attribution 3.0 Unported Licence.

Introduction

Nanopores have been widely utilized as powerful tools for the detection and characterization of various molecules in aqueous environments. By monitoring changes in ionic current during molecular translocation through a nanoscale pore, structural and electrical properties of individual molecules can be probed at the single-molecule level. Furthermore, recent advances in signal processing and data analysis, including machine learning (ML) and artificial intelligence (AI), have continuously improved the molecular discrimination capability of nanopore sensing.[1–3] Owing to these advantages, nanopore sensing has been widely extended to the analysis and discrimination of various molecules, ranging from nucleic acids for DNA sequencing applications[4,5] to proteins,[6,7] viruses,[8] environmental contaminants,[9,10] and food-related compounds,[11,12] and its potential applications in biomedical and related fields have been actively explored.

As the number of target molecular species increases, improving measurement throughput has become an important practical requirement. One of the most effective approaches to address this issue is to integrate nanopores into arrays and perform parallel measurements. In the field of biological nanopores, massively parallel measurements have already been realized in commercial devices developed by Oxford Nanopore Technologies, such as MinION and PromethION, which integrate hundreds to hundreds of thousands of nanopores.[5,13]

Meanwhile, several examples of nanopore integration and parallel measurement techniques for solid-state nanopores have also been reported. These include current measurement using microfluidic-integrated nanopore membranes,[14–18]

[a] Department of Biological Sciences, Graduate School of Science, The University of Tokyo, Tokyo, 113-0033, Japan. E-mail: i-yanagi@g.ecc.u-tokyo.ac.jp, uemura@bs.s.u-tokyo.ac.jp
[b] Hitachi Information & Telecommunication Engineering, Ltd, Yokohama, 220-6122, Japan
[c] Department of Electronics and Electrical Engineering, Keio University, Yokohama, 223-8522, Japan
[d] Healthcare Innovation Center, Research & Development Group, Hitachi, Ltd, Tokyo, 185-8603, Japan

Open Access Article. Published on 06 May 2026. Downloaded on 5/27/2026 1:15:12 PM.
This article is licensed under a Creative Commons Attribution 3.0 Unported Licence.

simultaneous recording from two nanopores integrated on a silicon chip,[19] concurrent nanopore formation on two membranes by dielectric breakdown,[20] low-cost microcontroller-based fabrication of nanopores,[21] wafer-scale fabrication of nanopore arrays,[22–24] high-density nanopore formation using microscale liquid contacts,[25] and multichannel current recording using arrayed quartz capillaries.[26] In addition, current amplifier systems capable of simultaneously measuring up to 16 nanopores (e16-HC) have recently become available from elements.[23] However, in terms of integration density and operational usability, there remains room for further development and improvement.

Beyond improving throughput, parallel nanopore measurements are also expected to play an important role in enhancing molecular discrimination performance. In solid-state nanopores, pore-to-pore variability is widely recognized as difficult to avoid.[27] Even when nanopores are fabricated with similar nominal diameters, subtle differences in geometry and surface charge can lead to substantial variations in molecular capture and transport behavior. Consequently, current-blockade characteristics can vary among individual nanopores, even for the same target molecule. This variability leads to pore-dependent discrimination performance. In addition, classification models trained using data from a specific pore often exhibit limited transferability to other pores.

Parallel nanopore array measurements are expected to provide an effective solution to these challenges. Simultaneous measurements of multiple nanopores under identical conditions allow statistical learning that incorporates pore-to-pore variability, thereby improving the robustness and generalizability of classification models. In addition, array-based measurements enable the simultaneous acquisition of multiple parameter dependencies, such as pore diameter, applied voltage, and electrolyte conditions (*e.g.*, salt species, concentration, and pH). These parameter-dependent features may further contribute to improving classification performance.[6]

In response to these increasing demands for array-based measurements, we developed a 16-channel solid-state nanopore array measurement system that enables integrated, parallel nanopore formation by dielectric breakdown and subsequent ionic current recording. The system supports both pulsed-voltage-induced dielectric breakdown (MPVI)[28] and controlled dielectric breakdown (CBD) under constant-voltage bias[29] for nanopore formation, enabling the fabrication of nanopore arrays with a wide range of diameters. To validate the performance of the developed system, we fabricated nanopore arrays with diameters of approximately 1–2 nm using MPVI and larger nanopore arrays with diameters of approximately 8–10 nm using CBD, and measured ionic current blockades during the translocation of single-stranded DNA and double-stranded DNA through the corresponding nanopores. By statistically analyzing nanopore formation characteristics and ionic current blockade signals across multiple channels, we evaluated variability and pore-size-dependent features that would be difficult or cumbersome to characterize using conventional single-pore measurements.

Experimental

Overview of the 16-channel solid-state nanopore array measurement system

A schematic diagram of the developed 16-channel solid-state nanopore array measurement system is shown in Fig. 1. The system consists of a flow cell incorporating membrane chips, an Ag/AgCl electrode array, a measurement circuit board, and a personal computer for parameter control and data acquisition. The flow cell and the circuit board were enclosed in a common Faraday cage. In addition, the circuit board was further shielded by a dedicated Faraday cage to suppress electromagnetic interference from the circuit board to the electrodes and flow cell. A detailed view of the flow cell and electrode array is shown on the right side of Fig. 1. The electrode array consists of a total of 32 Ag/AgCl electrodes, comprising 16 *cis*-side and 16 *trans*-side electrodes, which ensure electrical contact with the aqueous solutions on both sides of each nanopore. The flow cell is composed of three components: a top flow cell, a bottom flow cell, and a spacer. Sixteen membrane chips are mounted between the bottom flow path (*cis* chamber) and the top flow path (*trans* chamber) *via* O-ring gaskets. Schematic illustrations of the assembled flow cell and photographs of the membrane chips are provided in the SI (see SI-1).

Preparation of membrane chips, electrolyte solutions, and DNA samples

Two types of silicon nitride (SiN) membranes were used in this study: a 5 nm-thick membrane fabricated using a poly-Si sacrificial layer process and a 14 nm-thick membrane fabricated using an SiO_2 sacrificial layer process. The detailed fabrication processes have been described elsewhere.[30,31] The chips were cleaned and hydrophilized with piranha solution ($H_2O_2 : H_2SO_4$ = 1 : 3) for 3 min, followed by mounting onto the flow cell. Subsequently, the flow paths connected to each of the 16 membranes were filled with electrolyte solutions. In this study, three types of aqueous solutions with different pH values were used: 1 M KCl solutions with pH of 7.5, 8.7, and 12.7. The pH of each solution was adjusted by adding KOH to a 1 M KCl solution containing 10 mM Tris–HCl and 1 mM EDTA (pH 7.5). For molecular detection experiments based on nanopore translocation, 60 mer single-stranded DNA, $poly(dT)_{60}$ (Nihon Gene Research Laboratories, Inc.), and 400 bp double-stranded DNA were used as target molecules. The 400 bp dsDNA was prepared by PCR amplification of a specific region of λDNA (NIPPON GENE CO., LTD., Japan). Details of the preparation procedures are described in our previous report.[32]

 This journal is © The Royal Society of Chemistry 2026

Open Access Article. Published on 06 May 2026. Downloaded on 5/27/2026 1:15:12 PM.
This article is licensed under a Creative Commons Attribution 3.0 Unported Licence.

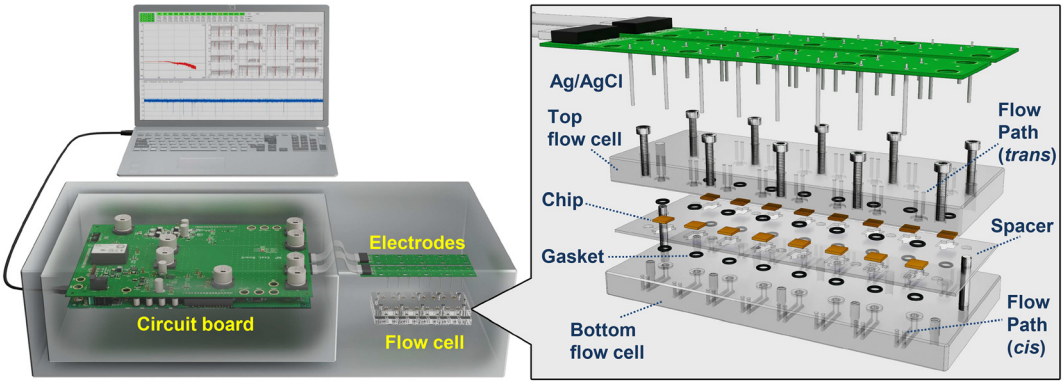

Fig. 1 Schematic of the 16-channel solid-state nanopore array measurement system. (Left) Overview of the system configuration, including the PC for control and data acquisition, the circuit board, the electrode array, and the flow cell. The flow cell and circuit board were housed in a common Faraday cage, and the circuit board was additionally shielded to reduce electromagnetic interference. (Right) Exploded view of the flow cell assembly and electrode array. Sixteen membrane chips are individually mounted between the *cis* and *trans* flow paths *via* O-ring gaskets. The electrode array comprises 32 Ag/AgCl electrodes (16 *cis*-side and 16 *trans*-side), enabling independent electrical access to each nanopore.

System architecture

Fig. 2 shows the architecture of the 16-channel solid-state nanopore array measurement system. The system consists of sixteen identical channel units and a central control field-programmable gate array (FPGA). Each channel unit comprises two modules: a nanopore fabrication module, and a readout module for measuring ionic currents through the fabricated nanopore. In the nanopore fabrication module, voltages of up to ±24 V can be applied through DAC1 connected to a high-voltage controller (HV ctrl), and the ionic current is converted into a voltage signal using a transimpedance amplifier with a feedback resistance of 500 kΩ. In the readout module, voltages of up to ±2 V are applied through DAC2 connected to a trans voltage controller (Trans V ctrl), and ionic currents are measured using transimpedance amplifiers with feedback resistances of 100 MΩ or 1 GΩ. All signals are digitized by ADCs and recorded. In this study, a feedback resistance of 100 MΩ was used in the readout module to ensure a wider measurement bandwidth. The sampling frequency was set to 50 kHz. Voltage application to the *cis* chamber is also possible *via*

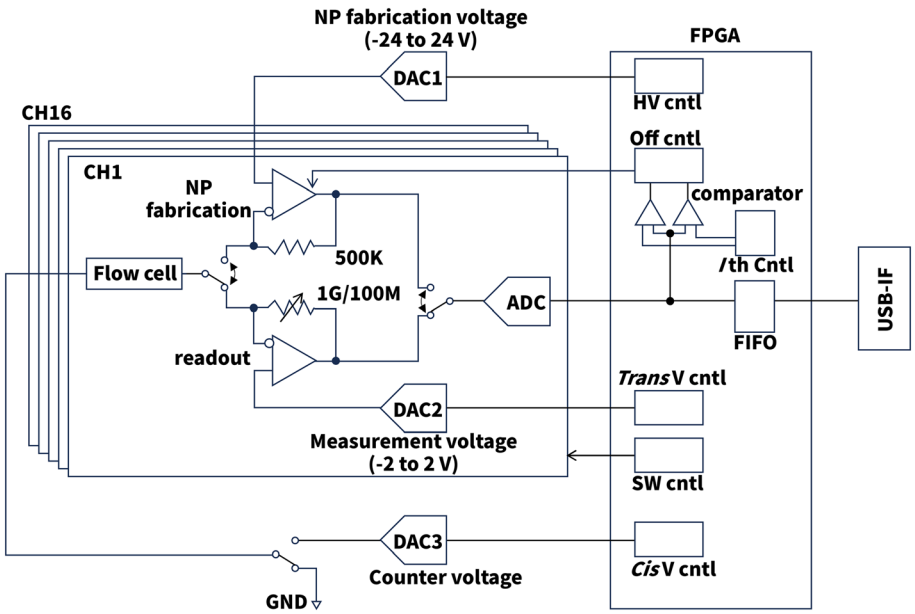

Fig. 2 Architecture of the 16-channel solid-state nanopore array system. Diagram of the circuit configuration consisting of 16 identical channel units and a central control FPGA. Each unit contains a nanopore fabrication module and a readout module for ionic current measurement. In the fabrication module, voltages up to ±24 V are applied *via* DAC1, and currents are measured with a 500 kΩ transimpedance amplifier. In the readout module, voltages up to ±2 V are applied *via* DAC2, and currents are measured with a 100 MΩ or 1 GΩ transimpedance amplifier. A comparator in the FPGA monitors the current and triggers voltage shutdown once the current exceeds a preset threshold (I_{th}) during CBD. Signals are digitized by ADCs and transferred *via* USB.

Open Access Article. Published on 06 May 2026. Downloaded on 5/27/2026 1:15:12 PM. This article is licensed under a Creative Commons Attribution 3.0 Unported Licence.

DAC3; however, the *cis* chamber was connected to ground in all measurements reported in this paper. The system is powered by a 5 V DC supply. Data acquisition and communication are managed by custom-developed control software *via* a USB 2.0 connection. A representative screenshot of the software is provided in the SI (see SI-2). The main components mounted on the circuit board are summarized in Table S1 in the SI (see SI-3).

The nanopore fabrication module supports two fabrication methods: pulsed-voltage-induced dielectric breakdown (MPVI)[28] and constant-voltage-controlled dielectric breakdown (CBD).[29] In both methods, simultaneous nanopore fabrication is possible in all 16 channels. In the MPVI method, high-voltage pulses are applied to the membrane through DAC1. After each pulse, a low voltage is applied to the membrane *via* DAC2, and the formation of the nanopore and its size are evaluated based on the resulting ionic current. In the CBD method, a constant high voltage is applied to the membrane *via* DAC1 while the transmembrane current is continuously monitored, and the voltage application is terminated when the measured current exceeds a preset threshold value. In this method, to minimize the delay between the transmembrane current reaching the threshold value and the termination of the voltage application, the voltage is switched off prior to current data recording. A comparator is implemented in the FPGA, and when the current exceeds the threshold specified by the I_{th} controller (I_{th} cntl), the OFF controller (OFF cntl) immediately terminates the voltage output. The delay time between the transmembrane current reaching the threshold and voltage shutdown is determined by the total processing time of the ADC, comparator, and OFF cntl, and is approximately 60 μs.

Estimation of nanopore diameter

The diameters of the fabricated nanopores in this study were estimated using the following equation,[33,34]

$$G = \frac{I}{V} = \sigma\left(\frac{4h_{\mathrm{eff.}}}{\pi\phi^2} + \frac{1}{\phi}\right)^{-1}, \quad (1)$$

where h_{eff} is the effective height of the nanopore and ϕ is the nanopore diameter. The conductivity σ was determined from measurements at 21 °C and was 0.105 S cm^{-1} for 1 M KCl (pH 7.5), 0.110 S cm^{-1} for 1 M KCl (pH 8.7), and 0.123 S cm^{-1} for 1 M KCl (pH 12.7). The effective height h_{eff} was set to 11 nm for 14 nm-thick SiN membranes and 1.7 nm for 5 nm-thick SiN membranes, according to previously reported values.[32,35,36]

Procedure for detection and analysis of current blockade signals

Detection and analysis of current blockade signals in the acquired current trace data were performed using a custom Python script. First, throughout the entire analysis window, contiguous segments in which the current fell below $I_{base} - k\sigma$ were extracted as event candidates. Here, I_{base} was defined as the 80th percentile value of the current in the analysis window, σ = 1.4826 × MAD, MAD was calculated from data above the 60th percentile as median($|x_i$ - median(x)|), and k was set to 8. All event analyses in this study were performed using these parameters. Next, the dwell time (Δt) for each event was defined as 20 μs × the number of sampling points in the contiguous segment during which the current remained below $I_{base} - k\sigma$. Segments with Δt shorter than 0.1 ms (fewer than five sampling points) were excluded from the event candidates because they were likely to represent noise. Subsequently, for each event, a local baseline was re-estimated from a 1.0 ms interval before the event onset. The current blockade amplitude, ΔI, was defined as the difference between this local baseline and the minimum current value during the event. Events with $\Delta I < 0.1$ nA were also excluded because such signals were considered likely to include noise-derived fluctuations. The extracted events were then used to construct scatter plots based on their Δt and ΔI values.

Results and discussion

Nanopore fabrication by MPVI and detection of ssDNA translocation through the nanopores

First, we discuss nanopore formation by MPVI using the developed parallel array measurement system, as well as the detection of translocation events of poly(dT)$_{60}$ through the fabricated nanopores. In this section, a 5 nm-thick SiN membrane and 1 M KCl (pH 7.5) were used. The characteristics of nanopore formation by MPVI are shown in Fig. 3, and a detailed flowchart of the MPVI procedure is provided in the SI (see SI-4).

MPVI consists of a nanopore generation process (Fig. 3(a)) and a subsequent pore-widening process (Fig. 3(b)).[37] In the generation process, the pulse voltage was initially set to 4.5 V. The initial pulse width was 1 ms, and the pulse duration was increased logarithmically as the number of applied pulses increased. After each pulse, the transmembrane current was measured at 0.4 V. When the current exceeded 200 pA (I_{th}), nanopore generation was considered complete and further pulse application to that channel was discontinued. Alternatively, if the cumulative pulse duration ($t_{sum} = \sum t_{pulse}$) reached 1 s in channels where nanopores had not yet been generated, the pulse voltage was increased in 0.5 V steps, and the pulse sequence was repeated at the higher voltage. Following this procedure, nanopores were successfully generated across all 16 channels with pulse voltages ranging from 4.5 V to 6 V, as shown in Fig. 3(a). Three channels (ch. 1, 7, 15) opened at 4.5 V; seven channels (ch. 2, 3, 8, 10, 13, 14, 16) at 5 V; five channels (ch. 4, 5, 6, 9, 11) at 5.5 V; and one channel (ch. 12) at 6 V.

In the nanopore-widening process, 2.8 V pulses were applied. After each pulse, the transmembrane current was measured at 0.1 V, and when the current exceeded 500 pA (I_{th}), the widening process was regarded as complete. This threshold corresponds to an estimated nanopore diameter of approximately 1.28 nm, as calculated from eqn (1). If the

 This journal is © The Royal Society of Chemistry 2026

Open Access Article. Published on 06 May 2026. Downloaded on 5/27/2026 1:15:12 PM.
This article is licensed under a Creative Commons Attribution 3.0 Unported Licence.

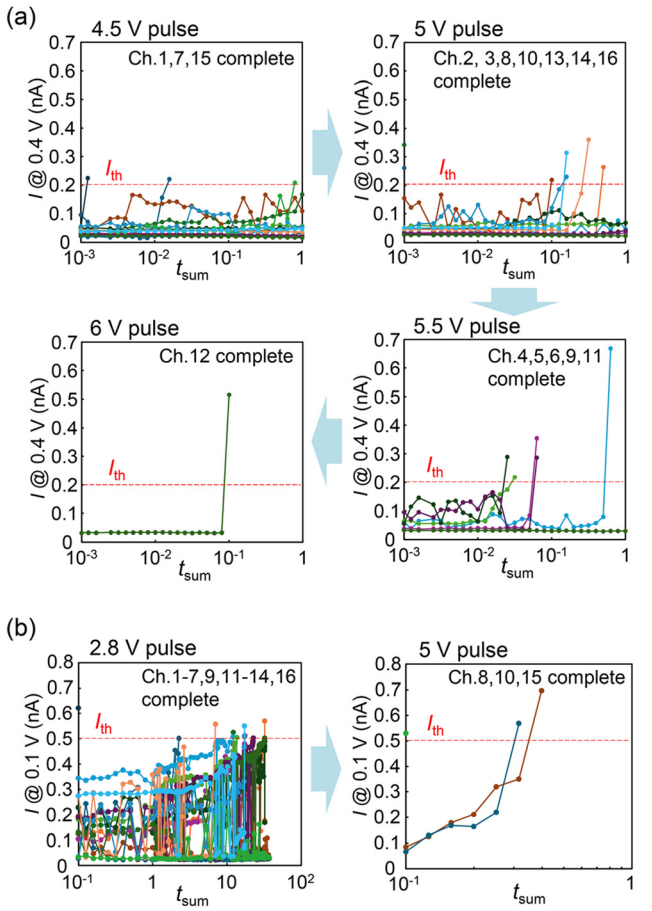

Fig. 3 Parallel nanopore fabrication by MPVI across 16 channels. (a) Nanopore generation process. The current measured at 0.4 V after each voltage pulse is plotted as a function of cumulative pulse duration (t_{sum}). The pulse voltage was incrementally increased from 4.5 V to 6 V in 0.5 V steps when necessary. Further pulse application was discontinued when the current exceeded 200 pA (I_{th}). (b) Nanopore widening process. The current measured at 0.1 V after each voltage pulse is plotted as a function of t_{sum}. Widening pulses of 2.8 V were applied and terminated when the current exceeded 500 pA (I_{th}). For channels not completed at 2.8 V, the pulse voltage was increased to 5 V to complete widening.

cumulative pulse duration reached 37 s in channels where the current at 0.1 V had not yet reached I_{th}, the pulse voltage for those channels was switched to 5 V to continue the widening process. Following this procedure, nanopore widening was completed at 2.8 V in 13 channels, while the remaining three channels were widened at 5 V, as shown in Fig. 3(b).

It is worth noting that, according to our previous study, thinner membranes undergo dielectric breakdown at lower voltages and yield smaller nanopores in the MPVI nanopore generation process.[38] Therefore, the thin SiN membrane used in this study (5 nm thick) is well suited for the formation of small nanopores, as demonstrated here. Indeed, at the end of the nanopore generation process, the current at 0.1 V was below the target value of 500 pA (corresponding to a pore diameter of 1.28 nm) for all nanopores. Consequently, no nanopores substantially larger than the target size were formed after completion of MPVI, resulting in small variation in nanopore size.

Subsequently, the solution in each *cis* chamber was replaced with 1 M KCl (pH 7.5) containing 10 nM poly(dT)$_{60}$. A bias voltage of 0.1 V was then applied to each *trans* chamber, and ionic currents were recorded in parallel across all channels. Representative 10 s current traces for each channel are shown in Fig. 4(a). Examples of typical blockade events are enlarged and shown in Fig. 4(b). The estimated nanopore diameters (ϕ), calculated from the baseline current using eqn (1), are indicated at the top of each trace in Fig. 4(a). Although all nanopores exhibited currents exceeding 500 pA at 0.1 V after the widening process, the baseline currents of several channels (ch. 08, 09, 10, and 13) decreased markedly after solution exchange. This decrease may be attributed to partial or complete clogging of the nanopores by ssDNA or nanobubbles. Zapping at ±1 V was attempted for these channels, but no recovery of the current was observed.

In contrast, three channels (ch. 02, 07, and 15) exhibited baseline currents exceeding 1 nA at 0.1 V, which were substantially higher than those measured immediately after the widening process. This increase suggests that the nanopores in these channels further enlarged after the widening step. A plausible explanation is that electrostatic charge generated on the surface of the flow cell during handling for solution exchange induced additional voltage stress across the membrane,[39,40] leading to further enlargement of the nanopores. In the case of channel 13, the estimated nanopore diameter was 1.34 nm, which is nominally sufficient to allow translocation of poly(dT)$_{60}$. However, only a very small number of translocation events were observed in this channel. One possible explanation is that the nanopore possesses an asymmetric or elliptical geometry, in which the minor axis is substantially smaller than the estimated effective diameter, thereby hindering ssDNA translocation.

Scatter plots of dwell time (Δt) *versus* blockade amplitude (ΔI), together with the corresponding histograms, are shown in Fig. 5. ΔI was defined as the maximum current-blockade value observed in each event, as shown in Fig. 4(b). The ΔI histograms were smoothed using kernel density estimation (KDE), and the highest peak of the smoothed distribution was defined as the peak blockade amplitude (ΔI_P). The Δt and ΔI values corresponding to the point of highest density in the scatter plot were also defined as Δt_D and ΔI_D, respectively, and these parameters, together with the estimated nanopore diameter (ϕ), the number of events, and the event frequency for each channel, are summarized in Table S2 of the SI (see SI-5). In this study, measurements were performed at a sampling frequency of 50 kHz, and only events with $\Delta t \geq 100$ μs (*i.e.*, events comprising five or more sampling points) were plotted in each scatter plot. Therefore, when the (Δt_D, ΔI_D) values extracted from each scatter plot satisfy $\Delta t_D > 100$ μs, they can be regarded as representing a

Open Access Article. Published on 06 May 2026. Downloaded on 5/27/2026 1:15:12 PM.
This article is licensed under a Creative Commons Attribution 3.0 Unported Licence.

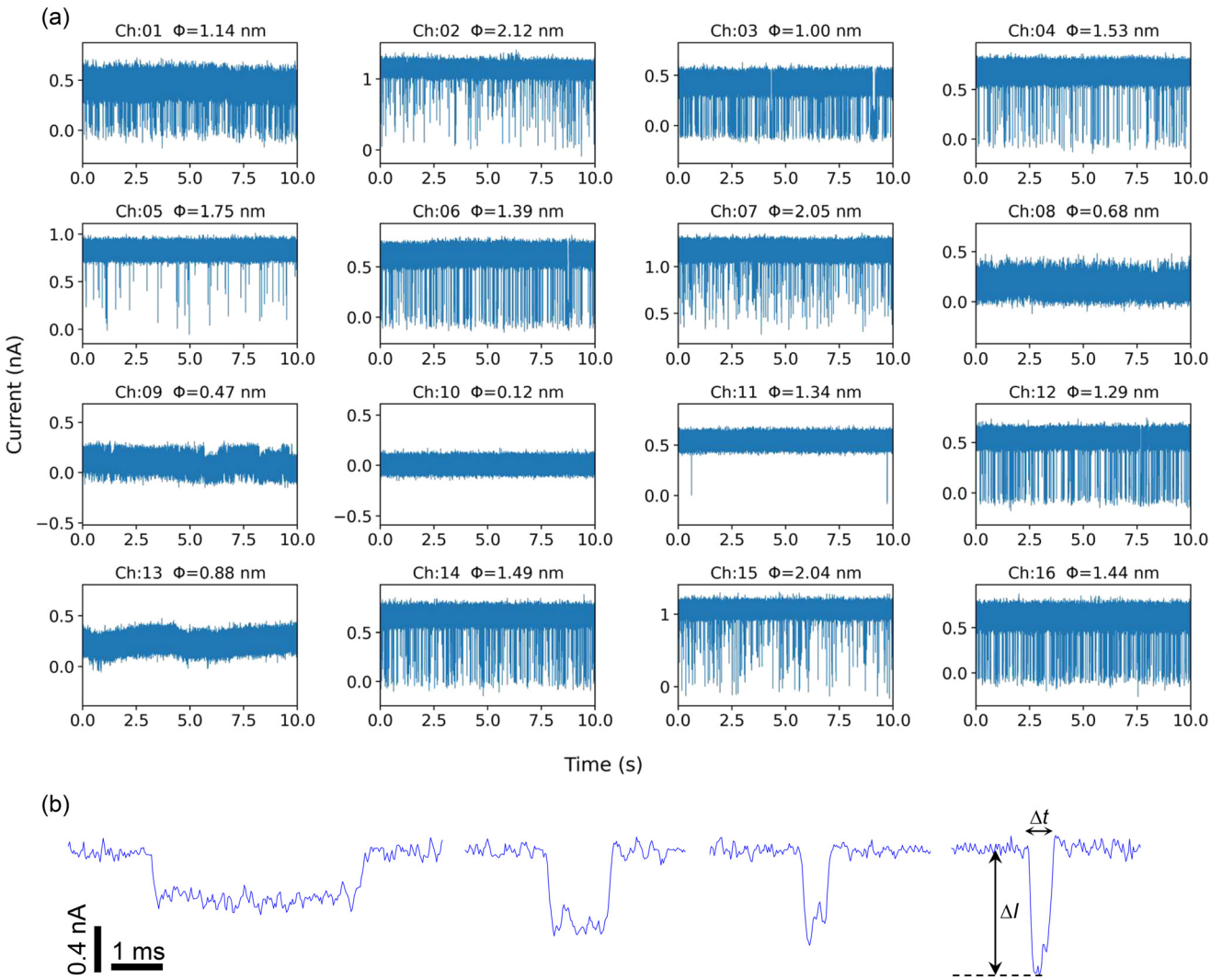

Fig. 4 Parallel measurement of ionic currents through 16 nanopores during poly(dT)$_{60}$ translocation. (a) Representative 10 s ionic current traces recorded in parallel from all 16 channels at 0.1 V in 1 M KCl (pH 7.5) containing 10 nM poly(dT)$_{60}$. Nanopore diameters (ϕ) estimated using eqn (1) are labeled for each channel. (b) Enlarged examples of typical current-blockade events.

local maximum point in that scatter plot. In contrast, when Δt_D = 100 μs, the actual local maximum point may lie in the region of $\Delta t_D < 100$ μs. Table S5 shows that $\Delta t_D > 100$ μs for all channels except channel 15, whereas channel 15 showed Δt_D = 100 μs. Therefore, for channel 15, the actual local maximum point may be located in the region of $\Delta t < 100$ μs. As for Channels 08, 09, 10, 11 and 13, fewer than 100 translocation events were detected; therefore, these channels were excluded from further quantitative analysis and subsequent discussion.

Fig. 6 presents the dependence of Δt_D, ΔI_D, and event frequency on the nanopore diameter (ϕ). The relationship between Δt_D and ϕ is shown in Fig. 6(a). Δt_D increased as ϕ decreased below approximately 1.75 nm, reaching about 10 ms at a nanopore diameter of around 1 nm, nearly two orders of magnitude larger than that observed at around 2 nm. This pronounced increase in dwell time at smaller pore diameters is likely attributable to enhanced interactions between ssDNA and the nanopore wall as the confinement becomes stronger. In addition, the observed trend that Δt_D increases as ϕ estimated from the baseline current becomes smaller may also be taken as evidence that a single nanopore is likely to have been formed in each membrane by the present MPVI process. If multiple nanopores had formed in a membrane, a large total current could arise from several small pores rather than a single large pore. In such a case, ϕ estimated from the baseline current would appear large, whereas Δt_D would still be expected to remain large because the DNA would pass through small nanopores. It should be noted that the data point at ϕ = 1.14 nm (channel 1) showed a small Δt_D despite the small pore diameter. This is presumably because collision events, in which DNA approaches the nanopore and then moves away without passing through it, were dominant over DNA translocation events.

This journal is © The Royal Society of Chemistry 2026

Open Access Article. Published on 06 May 2026. Downloaded on 5/27/2026 1:15:12 PM.
This article is licensed under a Creative Commons Attribution 3.0 Unported Licence.

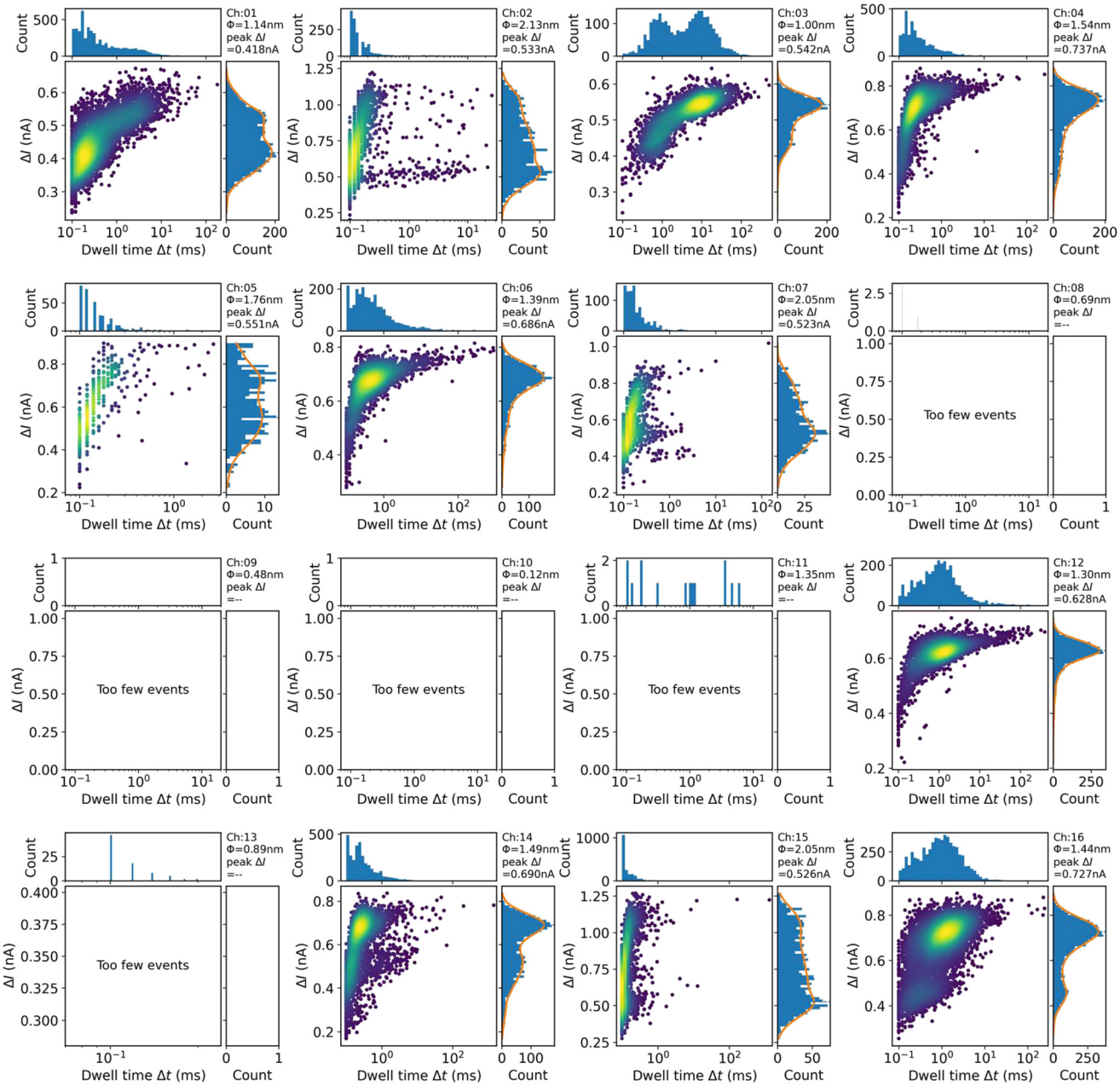

Fig. 5 Scatter plots and histograms of Δt and ΔI for poly(dT)$_{60}$ translocation across 16 channels. For each channel, the relationship between dwell time (Δt) and blockade amplitude (ΔI) is shown as a scatter plot, with the corresponding histograms shown in the upper and right panels. The ΔI distributions were smoothed using kernel density estimation (KDE), and the highest peak was defined as ΔI_P. Channels with fewer than 100 events (ch. 08–11, 13) are labeled as "too few events".

Fig. 6(b) presents the relationship between ΔI_D and ϕ. ΔI_D exhibited a non-monotonic dependence on ϕ, reaching a maximum at around 1.5 nm. For smaller pore diameters, ΔI_D decreased. This trend is consistent with our previous report[28] and may indicate that the effective diameter of ssDNA decreases to adjust to the size of the given nanopore. It should also be noted that the smaller ΔI_D value at ϕ = 1.14 nm (channel 1) than at ϕ = 1.00 nm (channel 3) is likely attributable to the predominance of collision events, as described above. For larger pore diameters, ΔI_D also decreased. This behavior is also consistent with the previous study by Kowalczyk *et al.*[41] and can be attributed to the increasing contribution of access resistance relative to pore resistance, which reduces the relative impact of DNA occupancy within the nanopore. The relationship between ΔI_P and nanopore diameter (ϕ) is also presented in the SI (see SI-6), where the above-mentioned trend is more clearly observed. Fig. 6(c) presents the dependence of event frequency on the nanopore diameter (ϕ). The event frequency ranged from approximately 3 to 60 events s^{-1} and did not exhibit a clear correlation with ϕ. Even among nanopores with similar diameters, noticeable differences in event

Open Access Article. Published on 06 May 2026. Downloaded on 5/27/2026 1:15:12 PM.
This article is licensed under a Creative Commons Attribution 3.0 Unported Licence.

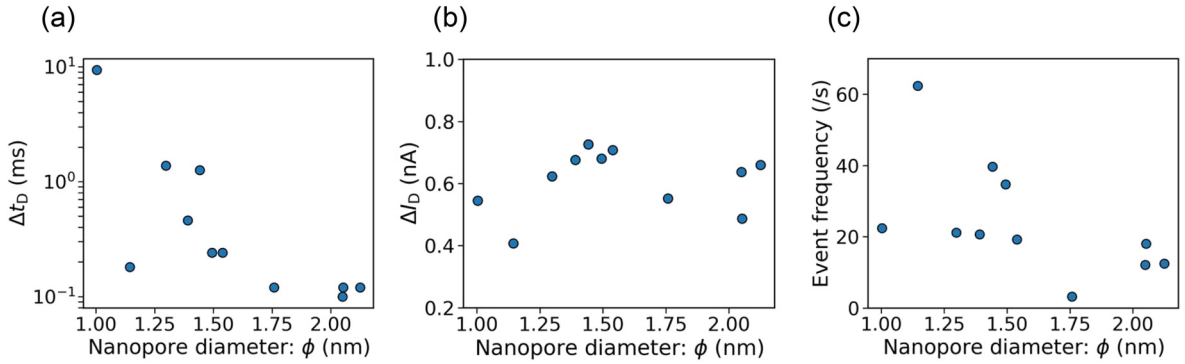

Fig. 6 Dependence of poly(dT)$_{60}$ translocation characteristics on nanopore diameter. (a) Δt_D *versus* ϕ. (b) ΔI_D *versus* ϕ. (c) Event frequency *versus* ϕ. Δt_D and ΔI_D are defined at the highest-density point of the Δt–ΔI scatter plots.

frequency were observed, which may reflect variations in the geometry or surface charge of the formed nanopores.

Nanopore fabrication by CBD and detection of dsDNA translocation through the nanopores

Next, we discuss nanopore fabrication by controlled breakdown (CBD) and the detection of dsDNA translocation through the fabricated nanopores. In this section, a 14 nm-thick SiN membrane was used. In nanopore fabrication, an aqueous solution of 1 M KCl (pH 12.7) was employed. This condition was adopted based on our previous report,[32] in which we demonstrated that the use of KCl solution with a pH of 12.7 enables rapid and stable formation of single nanopores with controllable sizes.

Fig. 7 shows the CBD characteristics of 16 nanopores fabricated in parallel. A voltage of −11 V was applied to each *trans* chamber, and the threshold current (I_{th}) for terminating voltage application was set to 700 nA. According to our previous report,[32] this voltage and threshold current are expected to produce nanopores with diameters of approximately 8–10 nm in the 14 nm-thick SiN membranes. Fig. 7(a) shows the full current trace of channel 11 as a representative example of CBD. A sudden increase in current is observed at approximately 11 s, indicating dielectric breakdown of the membrane. An enlarged view of the current trace from the onset of dielectric breakdown to the point at which the current reached the preset threshold (700 nA) is shown on the right side of the figure. When the current reached I_{th}, voltage application was automatically terminated within 60 μs, as described in the Experimental section, and the current immediately dropped to zero. The time at which the current abruptly increased from zero is referred to as the dielectric breakdown point, while the time at which the current reached I_{th} is referred to as the end-of-NP-fabrication point. The time interval between these two points is defined as t_w.

Fig. 7(b) shows the current traces of all 16 channels in the region between the dielectric breakdown point and the end-of-NP-fabrication point. In all channels, both the dielectric breakdown point and the end-of-NP-fabrication point can be clearly identified.

Fig. 7(c) presents a histogram of the time to breakdown, *i.e.*, the time at the dielectric breakdown point (t_B). Most breakdown times fell between 10 and 20 s, suggesting rapid formation of nanopores across the array. The Weibull plot of t_B is shown in Fig. 7(d). The cumulative failure probability $F(t)$ is defined as

$$F(t) = \frac{n(t)}{N}, \tag{2}$$

where N = 16 is the total number of membranes and $n(t)$ is the number of membranes that experienced dielectric breakdown by time t. According to the Weibull distribution derived from a weakest-link model,[42–46] $F(t)$ can be expressed as

$$F(t) = 1 - \exp\left[-\left(\frac{t}{\eta}\right)^{\beta}\right] \tag{3}$$

where β is the Weibull slope parameter and η is the characteristic time at which approximately 63% of the membranes have experienced dielectric breakdown. The experimental data in Fig. 7(d) are well fitted by eqn (3), yielding β = 4.387 and η = 16.214 s. These results indicate that the breakdown events in our experiment follow a weakest-link model, consistent with previous reports.[25,46,47]

Fig. 7(e) presents a histogram of t_w. For most channels, t_w is found to lie within the range of approximately 0.3–0.5 s. Fig. 7(f) shows overlaid current traces of all 16 channels from the dielectric breakdown point to the end-of-NP-fabrication point. For comparison, the time axis for each channel was normalized so that the interval between these two points was scaled to unity. Notably, immediately after dielectric breakdown, a current of approximately 50–100 nA was observed in all channels. The current then remained relatively constant for a certain period, and the rapid increase toward I_{th} occurred primarily in the latter portion of each trace. These current profiles likely reflect the nanopore formation dynamics. One possible interpretation is that little pore enlargement occurs for a certain period after dielectric breakdown; however, once the reaction process required for pore growth is triggered, it proceeds in an avalanche-like

 This journal is © The Royal Society of Chemistry 2026

Open Access Article. Published on 06 May 2026. Downloaded on 5/27/2026 1:15:12 PM.
This article is licensed under a Creative Commons Attribution 3.0 Unported Licence.

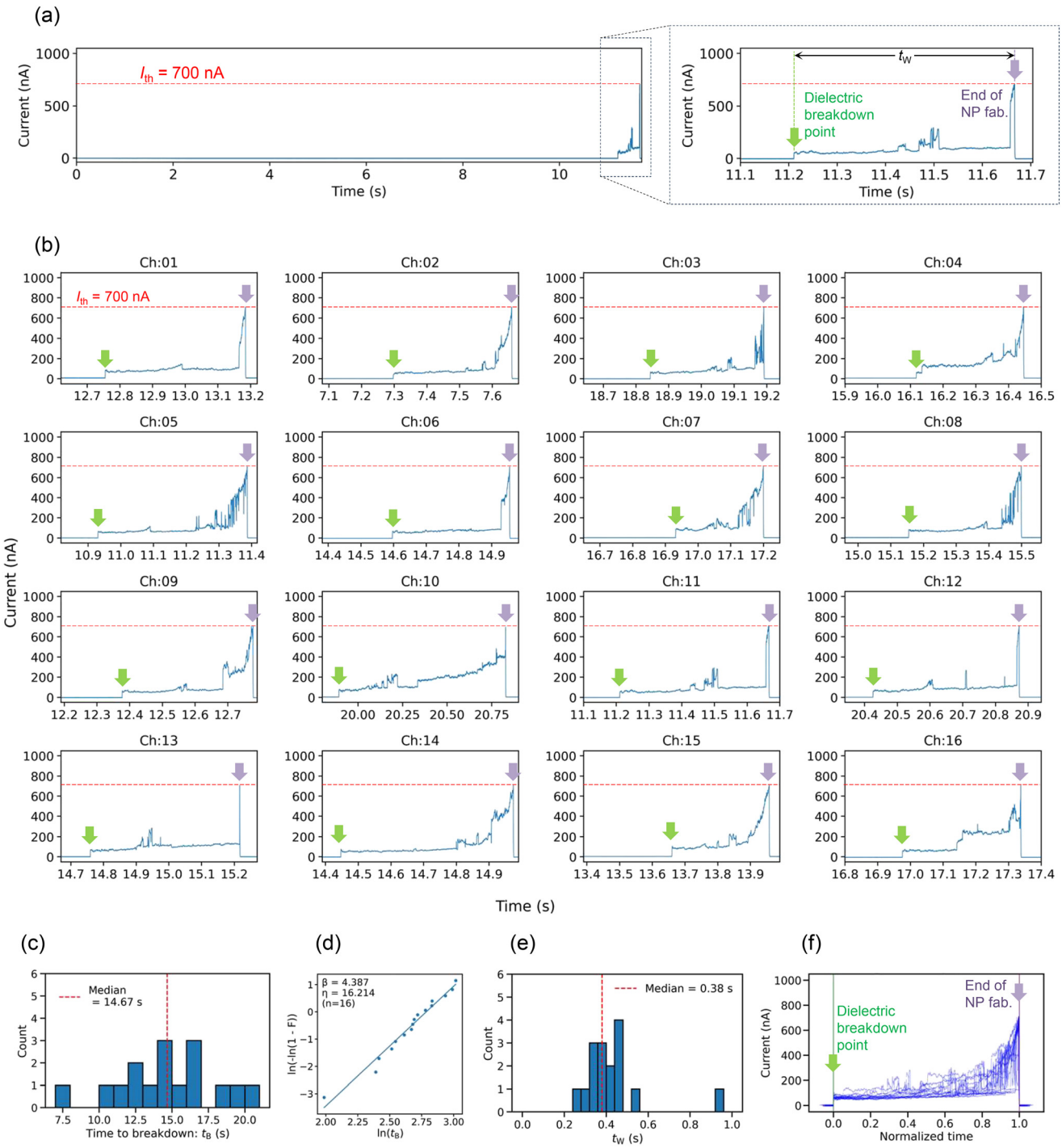

Fig. 7 Parallel nanopore fabrication by CBD across 16 channels. An aqueous solution of 1 M KCl (pH 12.7) was used, and −11 V was applied to each *trans* chamber. (a) Full current trace for channel 11 during CBD, with an enlarged view near the dielectric breakdown event. Voltage was terminated when the current reached 700 nA (I_{th}). (b) Current traces for all 16 channels from the dielectric breakdown point to the end-of-NP-fabrication point. (c) Histogram of the time to breakdown (t_B). (d) Weibull plot of t_B with a fit based on eqn (3). (e) Histogram of the time interval t_w between the dielectric breakdown point and the end-of-NP-fabrication point. (f) Overlaid normalized current traces from the dielectric breakdown point to the end-of-NP-fabrication point.

manner, leading to rapid expansion of the nanopore toward the preset threshold.

Fig. 8 shows the *I–V* characteristics of all channels after CBD (Fig. 8(a)) and a histogram of the nanopore diameters (ϕ) calculated from the current at 0.1 V using eqn (1) (Fig. 8(b)). The *I–V* curves exhibit nearly linear behavior for all channels. The nanopore diameters fall within the range of 8–10 nm for 13 of the 16 channels and within 8–9 nm for 12

Open Access Article. Published on 06 May 2026. Downloaded on 5/27/2026 1:15:12 PM.
This article is licensed under a Creative Commons Attribution 3.0 Unported Licence.

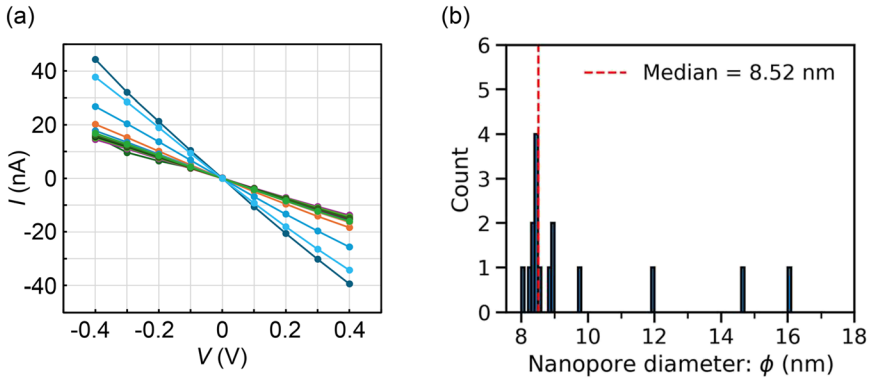

Fig. 8 *I–V* characteristics and estimated diameters of nanopores fabricated by CBD. (a) *I–V* curves of all 16 channels after CBD. (b) Histogram of nanopore diameters (ϕ) calculated from the current at 0.1 V using eqn (1).

channels, indicating tight size control in the fabrication process. These nanopore diameters were consistent with those expected from our previous report.[32] However, in 3 of the 16 channels, nanopores with diameters larger than approximately 12 nm were formed, which are noticeably larger than those of the other channels. These channels are ch. 4, ch. 16, and ch. 10 (listed in order of increasing diameter). A comparison of t_B, t_w, and the CBD current traces for these channels with those of the remaining channels did not reveal any clear distinguishing features. At present, no definitive explanation can be provided for this phenomenon. One possible interpretation is that, even after voltage application was terminated, relatively fragile and weakly bonded regions of SiN constituting the nanopore may have continued to undergo structural relaxation or collapse, resulting in the formation of larger nanopores compared with the other channels.

It should be noted that in our previous study,[32] TEM observation was performed after CBD on 14 nm-thick SiN membranes under almost the same conditions as those used here (application of −11 V to the *trans* chamber in 1 M KCl aqueous solution at pH 12.7, with I_{th} = 300–1000 nA). As a result, formation of a single nanopore was confirmed in all six membranes examined. Therefore, it is highly likely that a single nanopore was also formed in the present CBD experiments.

In addition, 16-channel parallel nanopore fabrication by CBD was also carried out on 20 nm-thick SiN membranes under the conditions of −18 V applied to the *trans* chamber in 1 M KCl aqueous solution at pH 12.7, and I_{th} = 600 nA, which were previously confirmed by TEM observation in our earlier study to yield a single nanopore in a membrane.[32] The results are shown in the SI (see SI-7). Fig. S5(c) in S7 shows the estimated diameters of the fabricated nanopores presented as box-and-whisker plots together with those for the 14 nm-thick SiN membranes shown in Fig. 8 in the main text. Excluding outliers, the variation in the fabricated nanopore diameters is very small for both the 20 nm-thick and 14 nm-thick membranes, remaining within 2 nm.

After completion of the nanopore-fabrication process for the 14 nm-thick SiN membranes, the solutions in each *cis* and *trans* chamber were replaced with 1 M KCl (pH 8.7) containing 10 nM dsDNA (400 bp).[32] A bias voltage of 0.2 V was then applied to each *trans* chamber, and ionic currents were recorded in parallel across all channels. Representative 10 s current traces for each channel are shown in Fig. 9(a). Examples of typical blockade events are enlarged and shown in Fig. 9(b). Each trace in Fig. 9(a) is labeled with the nanopore diameter (ϕ), calculated from the baseline current using eqn (1). Compared with the nanopore diameters estimated immediately after CBD, the diameters increased by approximately 1 nm on average. As also discussed in the previous section, this increase may be attributed in part to electrostatic charge generated on the surface of the flow cell during handling for solution exchange.[39,40] It can be seen from Fig. 9(a) that the baseline noise level, event frequency, and blockade amplitude differ among channels.

Scatter plots of dwell time (Δt) *versus* blockade amplitude (ΔI), together with the corresponding histograms, are shown in Fig. 10. ΔI_P (defined as the highest peak of the smoothed ΔI histogram), Δt_D and ΔI_D (defined as the Δt and ΔI values at the highest-density point in the Δt–ΔI scatter plot), the estimated nanopore diameter (ϕ), the number of events, and the event frequency for each channel are summarized in the SI (see SI-8). Δt_D was 100 μs for channels 4 and 8, but as in the discussion of the poly(dT)$_{60}$ nanopore translocation experiment above, the actual local maximum points for these channels may lie in the region of $\Delta t < 100$ μs. Many channels exhibit a peak in ΔI around 0.5–0.6 nA. At the same time, in some channels, a substantial number of events are observed at higher ΔI values above 1 nA, sometimes forming a distinct cluster in the scatter plot. This tendency is more frequently observed in channels with larger nanopore diameters (*e.g.*, ch. 04 and ch. 10), likely because larger pores increase the likelihood of folded DNA translocation or simultaneous passage of multiple DNA molecules, thereby leading to larger ΔI values. In addition, some channels showed a considerable number of events in the region of small ΔI values (around 0.1–0.2 nA). These events are considered not to be DNA

This journal is © The Royal Society of Chemistry 2026

Open Access Article. Published on 06 May 2026. Downloaded on 5/27/2026 1:15:12 PM.
This article is licensed under a Creative Commons Attribution 3.0 Unported Licence.

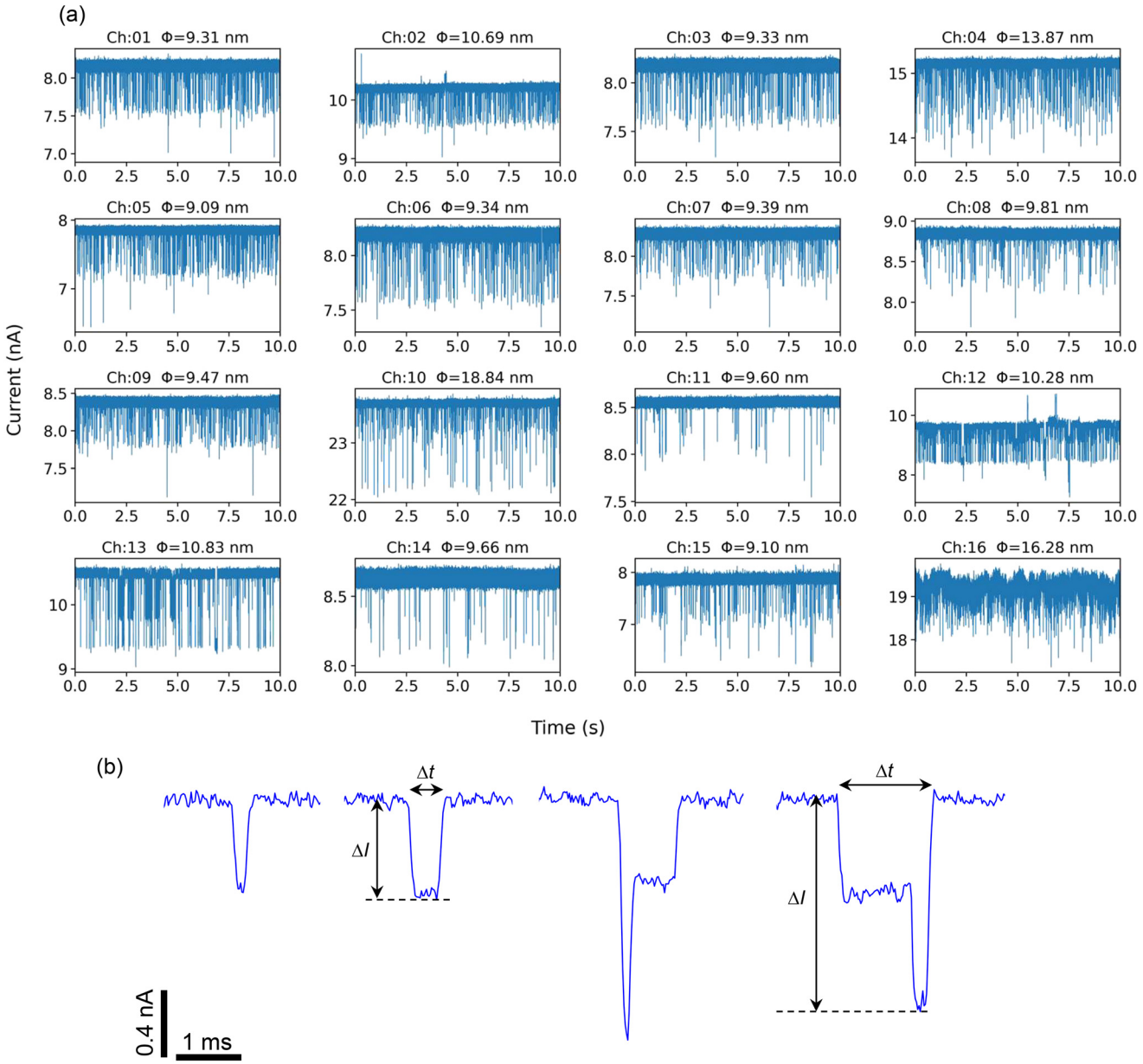

Fig. 9 Parallel measurement of ionic currents through 16 nanopores during dsDNA translocation. (a) Representative 10 s ionic current traces recorded in parallel from all 16 channels at 0.1 V in 1 M KCl (pH 8.7) containing 400 bp dsDNA. Nanopore diameters (ϕ) estimated using eqn (1) are labeled for each channel. (b) Enlarged examples of typical current-blockade events.

translocation events, but rather collision events, in which DNA approaches the vicinity of the nanopore and then moves away without passing through it.

Fig. 11 presents the dependence of Δt_D, ΔI_D, and event frequency on the nanopore diameter. For Δt_D, most channels exhibit similar values in the range of 0.1–0.2 ms, with no clear dependence on pore diameter. This can be attributed to the fact that the nanopores are sufficiently larger than the diameter of dsDNA; consequently, interactions between dsDNA and the pore wall are weaker than those in the smaller nanopores discussed in the previous section and do not significantly affect the translocation velocity even with moderate variations in pore diameter. For ΔI_D, the values are distributed within approximately 0.4–0.8 nA, again without a clear dependence on pore diameter. One possible source of this variation is differences in the effective pore height (h_{eff}) of the fabricated nanopores. As indicated by eqn (1), ΔI_D increases or decreases with an increase or decrease in h_{eff}, respectively. The relationship between ΔI_P and nanopore diameter (ϕ) is also presented in the SI (see SI-9), where no clear dependence on pore diameter is observed either. The event frequency likewise shows channel-to-channel variation regardless of pore diameter. Similar considerations to those discussed in the previous section may apply here; this variation likely reflects differences in pore geometry and surface charge among the fabricated nanopores.

Open Access Article. Published on 06 May 2026. Downloaded on 5/27/2026 1:15:12 PM.
This article is licensed under a Creative Commons Attribution 3.0 Unported Licence.

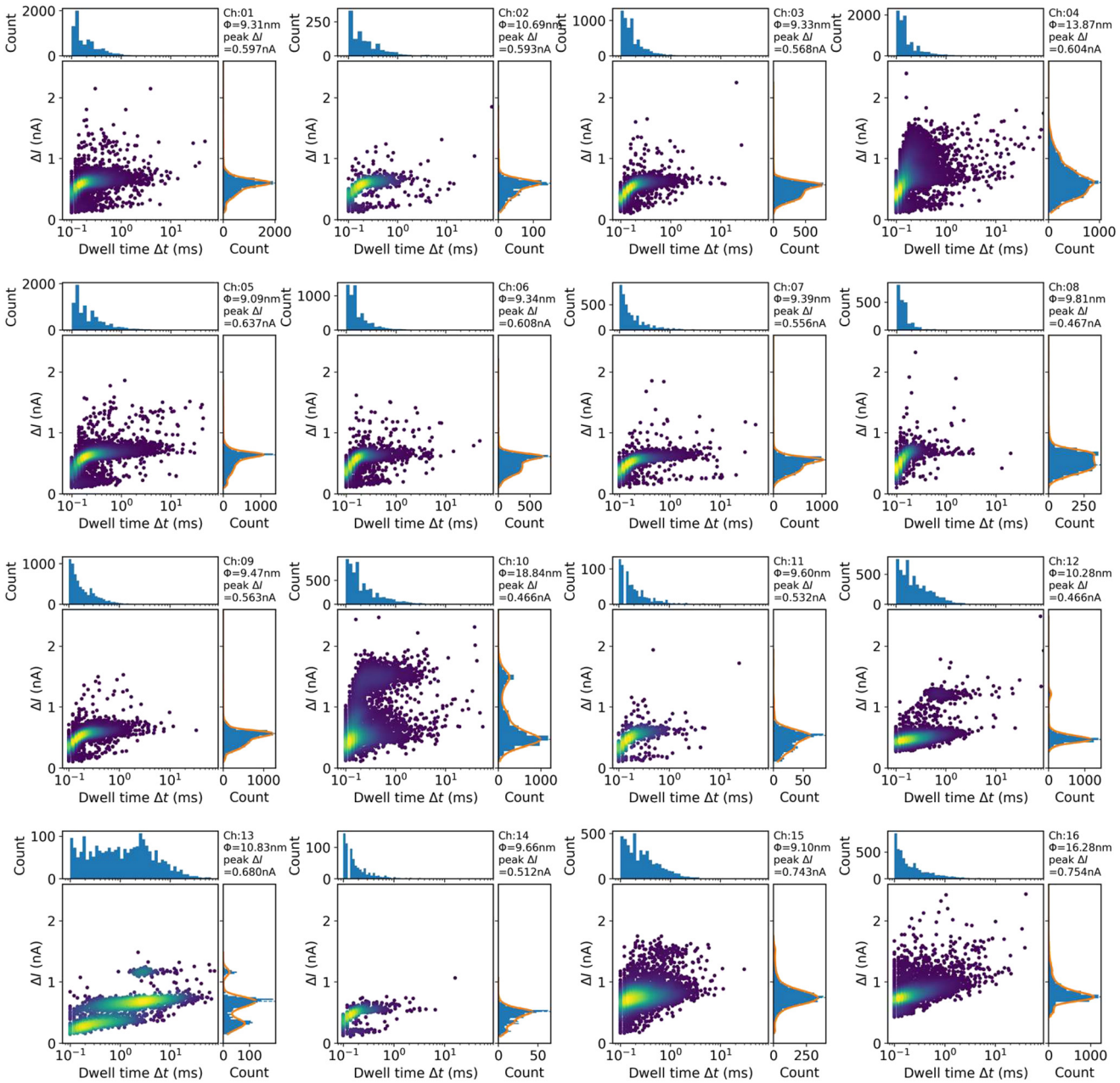

Fig. 10 Scatter plots and histograms of Δt and ΔI for dsDNA translocation across 16 channels. For each channel, the relationship between dwell time (Δt) and blockade amplitude (ΔI) is shown as a scatter plot, with the corresponding histograms shown in the upper and right panels. The ΔI distributions were smoothed using kernel density estimation (KDE), and the highest peak was defined as ΔI_P.

Evaluation of noise and inter-channel crosstalk during measurements

Finally, we present a detailed evaluation of current noise and inter-channel signal crosstalk during measurements using the 16-channel measurement system. SI (see SI-10) compares the ionic-current noise for nanopores formed in the 5 nm-thick and 14 nm-thick SiN membranes used in this study. The 14 nm-thick SiN membranes fabricated by the SiO_2 sacrificial layer process exhibited lower noise than the 5 nm-thick membranes fabricated by the poly-Si sacrificial layer process because of their lower capacitance, which is consistent with our previous report.[31]

SI (see SI-11) shows the open-input RMS current noise and the RMS current noise with nanopores connected, measured in the 16-channel measurement system. RMS current noise was measured for each channel under two conditions: all 16 channels active (16 ch active) and only one channel active at a time (1 ch active; the other 15 channels were disabled). No large differences in RMS current noise were observed among the channels, and almost no difference was found between the 16 ch active and 1 ch active conditions. In addition, Fig.

 This journal is © The Royal Society of Chemistry 2026

Open Access Article. Published on 06 May 2026. Downloaded on 5/27/2026 1:15:12 PM.
This article is licensed under a Creative Commons Attribution 3.0 Unported Licence.

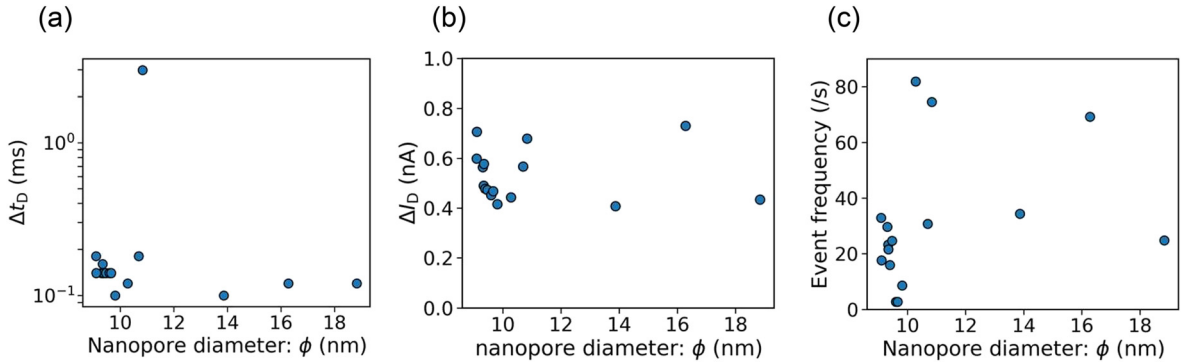

Fig. 11 Dependence of dsDNA translocation characteristics on nanopore diameter. (a) Δt_D *versus* ϕ. (b) ΔI_D *versus* ϕ. (c) Event frequency *versus* ϕ. Δt_D and ΔI_D are defined at the highest-density point of the Δt–ΔI scatter plots.

S8 in the SI (see SI-12) shows the enlarged current traces of adjacent channels in the experiment shown in the previous section (Fig. 9). As shown in the figure, when a blockade current was observed in one channel, no correlated fluctuation was observed in the adjacent channel, indicating the absence of inter-channel crosstalk in the blockade-current signal.

Conclusions

We developed a 16-channel solid-state nanopore array system for parallel nanopore fabrication and subsequent ionic current measurement through the formed pores. The system comprises a control and data acquisition computer, a custom circuit board, a 32-electrode Ag/AgCl array, and a flow cell integrating sixteen membrane chips. The circuit board incorporates sixteen channel units—each equipped with a nanopore fabrication module and an ionic current readout module—together with a central FPGA-based control unit. The fabrication module supports two nanopore formation methods: pulsed-voltage-induced dielectric breakdown (MPVI) and controlled dielectric breakdown (CBD) under constant-voltage bias.

To evaluate system performance, two experimental studies were carried out. In the first study, nanopores were fabricated in 5 nm-thick SiN membranes using MPVI, followed by detection of ssDNA ($poly(dT)_{60}$) translocation. Application of 4.5–6 V voltage pulses enabled nanopore formation in all 16 channels, and subsequent pulse application allowed controlled enlargement to pore diameters of approximately 1–2 nm. High-frequency current-blockade events were observed in 11 of the 16 channels. Analysis of the Δt–ΔI scatter plots across multiple nanopores revealed that the dwell time at the highest-density point (Δt_D) increased by up to two orders of magnitude as the nanopore diameter decreased from approximately 2 nm to 1 nm, reflecting enhanced interactions between $poly(dT)_{60}$ and the nanopore wall under stronger confinement. In addition, the corresponding ΔI_D was maximized at approximately 1.5 nm; this likely results from a balance between the effective diameter adaptation of ssDNA in smaller pores and the increasing contribution of access resistance relative to pore resistance in larger pores.

In the second study, nanopores were fabricated in 14 nm-thick SiN membranes using CBD, followed by detection of 400 bp dsDNA translocation. By applying −11 V with a cutoff current (I_{th}) of 700 nA, nanopore formation was completed within approximately 20 s in all 16 channels. Current traces during CBD indicated that pore enlargement remained limited shortly after dielectric breakdown, but once growth was initiated, the current increased rapidly toward the preset threshold, suggesting an avalanche-like pore expansion process. The resulting pore diameters were narrowly distributed across the array, with 12 of 16 pores within 8–9 nm and 13 of 16 within 8–10 nm, demonstrating tight size control across most channels. Using these fabricated nanopores, dsDNA translocation events were observed in all channels. Larger nanopores tended to exhibit a higher fraction of large-ΔI events, likely due to an increased probability of folded DNA translocation or the simultaneous passage of multiple DNA molecules.

These results demonstrate that the developed platform enables rapid and size-controlled parallel nanopore fabrication, along with stable and high-throughput molecular detection. Future work will focus on the discrimination of heterogeneous samples using the developed system. By incorporating pore-to-pore variation into statistical learning frameworks and by systematically varying pore diameter and solution conditions across channels, we will examine how much classification accuracy can be improved compared with conventional single-pore measurements.

In parallel, we plan to develop larger-scale arrays exceeding 16 channels to increase the amount of information obtained per measurement. Several challenges must be addressed to achieve this, and we believe the following two are particularly important. The first concerns the current flow-cell design. If we continue to use the current one-membrane-per-chip design, scaling the array to 64, 128, or more channels would cause the flow-cell size to increase substantially. In addition, introducing and exchanging aqueous solution for each membrane through individual flow paths by manual pipetting would become extremely

Open Access Article. Published on 06 May 2026. Downloaded on 5/27/2026 1:15:12 PM.
This article is licensed under a Creative Commons Attribution 3.0 Unported Licence.

cumbersome, making the system impractical from the standpoint of usability. Therefore, it will be necessary to shift from the current one-membrane-per-chip design to chips integrating multiple membranes to achieve miniaturization. In addition, a mechanism such as an automated dispensing system for introducing aqueous solution into individual flow paths will also be required to ensure the practical usability of a large-scale array system. Another challenge is the substantial increase in the volume of acquired data. Several approaches may be taken to address this issue. For example, channels exhibiting very few events or sample clogging could be identified at an early stage of measurement and excluded from data acquisition. Another approach would be to store the data while excluding the intervals between events. We believe that as the array size increases, new challenges will arise, but that addressing them one by one will be essential to enabling further scaling.

Conflicts of interest

There are no conflicts to declare.

Data availability

The data supporting this article are available in the main text and in the supplementary information (SI). The graphs in Fig. 6 and 11 were plotted using the data listed in the Tables S2 and S3, respectively.

Supplementary information is available. See DOI: https://doi.org/10.1039/d6lc00216a.

Acknowledgements

We thank Dr Rena Akahori of Hitachi for her valuable discussions and critical comments on the manuscript. This work was supported by JST, CREST (Grant no. JPMJCR2231) and JST, K-program (Grant no. JPMJKP23H2).

References

1 N. S. Shrikrishna and S. Gandhi, *J. Nanobiotechnol.*, 2025, **23**, 03762.
2 K. Xia, J. T. Hagan, L. Fu, B. S. Sheetz, S. Bhattacharya, F. Zhang, J. R. Dwyer and R. J. Linhardt, *Proc. Natl. Acad. Sci. U. S. A.*, 2021, **118**, e2022806118.
3 S. Dutt, B. Karawdeniya, Y. M. Bandara and P. Kluth, *Future Sci. OA*, 2024, **10**, 2340882.
4 M. Jain, H. E. Olsen, B. Paten and M. Akeson, *Genome Biol.*, 2016, **17**, 239.
5 M. Jain, S. Koren, K. H. Miga, J. Quick, A. C. Rand, T. A. Sasani, J. R. Tyson, A. D. Beggs, A. T. Dilthey, I. T. Fiddes, S. Malla, H. Marriott, T. Nieto, J. O'Grady, H. E. Olsen, B. S. Pedersen, A. Rhie, H. Richardson, A. R. Quinlan, T. P. Snutch, L. Tee, B. Paten, A. M. Phillippy, J. T. Simpson, N. J. Loman and M. Loose, *Nat. Biotechnol.*, 2018, **36**, 338–345.
6 R. Akita, A. Lysenko, K. A. Boroevich, T. Yokota, D. Kawai, R. Iizuka, T. Tsunoda and S. Uemura, *Chem. Sci.*, 2025, **16**, 18607–18615.
7 M. Afshar Bakshloo, J. J. Kasianowicz, M. Pastoriza-Gallego, J. Mathé, R. Daniel, F. Piguet and A. Oukhaled, *J. Am. Chem. Soc.*, 2022, **144**, 2716–2725.
8 M. Taniguchi, S. Minami, C. Ono, R. Hamajima, A. Morimura, S. Hamaguchi, Y. Akeda, Y. Kanai, T. Kobayashi, W. Kamitani, Y. Terada, K. Suzuki, N. Hatori, Y. Yamagishi, N. Washizu, H. Takei, O. Sakamoto, N. Naono, K. Tatematsu, T. Washio, Y. Matsuura and K. Tomono, *Nat. Commun.*, 2021, **12**, 3726.
9 X. Wei, A. Choudhary, L. Y. Wang, L. Yang, M. J. Uline, M. Tagliazucchi, Q. Wang, D. Bedrov and C. Liu, *Sci. Adv.*, 2024, **10**, eadp8134.
10 X. Lu, D. Zhong, Q. An, L. Kang, N. Fan, J. Cao, R. Li, Q. Cao, Y. Zhou, X. Du, S. Yan, J. Li, X. Qu and Y. Wang, *ACS Nano*, 2025, **19**, 37281–37295.
11 P. Fan, Z. Cao, S. Zhang, Y. Wang, Y. Xiao, W. Jia, P. Zhang and S. Huang, *Nat. Commun.*, 2024, **15**, 1969.
12 Y. Xiao, X. Du, L. Zhao, X. Dai, L. Qian, S. Zhang, P. Zhang, S. Huang and K. Wang, *ACS Nano*, 2026, **20**, 2740–2751.
13 Y. Wang, Y. Zhao, A. Bollas, Y. Wang and D. Y. Wang, *Nat. Biotechnol.*, 2021, **39**, 1348–1365.
14 T. Jain, B. C. Rasera, R. J. S. Guerrero, J.-M. Lim and R. Karnik, *J. Phys.: Condens. Matter*, 2017, **29**, 484001.
15 T. Jain, R. J. S. Guerrero, C. A. Aguilar and R. Karnik, *Anal. Chem.*, 2013, **85**, 3871–3878.
16 R. Tahvildari, E. Beamish, K. Briggs, S. Chagnon-Lessard, A. N. Sohi, S. Han, B. Watts, V. Tabard-Cossa and M. Godin, *Small*, 2017, **13**, 1602601.
17 R. Tahvildari, E. Beamish, V. Tabard-Cossa and M. Godin, *Lab Chip*, 2015, **15**, 1407–1411.
18 P. D. Jones and M. Mierzejewski, *J. Micromech. Microeng.*, 2025, **35**, 045003.
19 I. Yanagi, R. Akahori, M. Aoki, K. Harada and K. Takeda, *Lab Chip*, 2016, **16**, 3340–3350.
20 M. Waugh, K. Briggs, D. Gunn, M. Gibeault, S. King, Q. Ingram, A. M. Jimenez, S. Berryman, D. Lomovtsev, L. Andrzejewski and V. Tabard-Cossa, *Nat. Protoc.*, 2020, **15**, 122–143.
21 Y. M. N. D. Y. Bandara, B. I. Karawdeniya, S. Dutt, P. Kluth and A. Tricoli, *Anal. Chem.*, 2024, **96**, 2124–2134.
22 L. Zhao, J. Wang, L.-S. Wu and X. Zhao, *Microsyst. Nanoeng.*, 2025, **11**, 129.
23 A. R. Chaudhuri, E. Beamish, B. Du Bois, P. Guell, A. Walikar, E. Vecchio, T. Vossen, A. Podkovskiy, W. Renckens, W. Botermans, S. Marion, H. Osman, P. Deshpande, S. Severi and P. Van Dorpe, *Proc. IEEE Int. Electron Devices Meet*, 2025, DOI: 10.1109/IEDM50572.2025.11353639.
24 H. K. Gatty, N. X. Chung, M. Zhang, I. Sychugov and J. Linnros, *Nanotechnology*, 2020, **31**, 355505.
25 C. E. Arcadia, C. C. Reyes and J. K. Rosenstein, *ACS Nano*, 2017, **11**, 4907–4915.
26 N. A. W. Bell, V. V. Thacker, S. Hernández-Ainsa, M. E. Fuentes-Perez, F. Moreno-Herrero, T. Liedl and U. F. Keyser, *Lab Chip*, 2013, **13**, 1859–1862.

This journal is © The Royal Society of Chemistry 2026

Open Access Article. Published on 06 May 2026. Downloaded on 5/27/2026 1:15:12 PM.
This article is licensed under a Creative Commons Attribution 3.0 Unported Licence.

27 B. Cressiot, S. J. Greive, M. Mojtabavi, A. A. Antson and M. Wanunu, *Nat. Commun.*, 2018, **9**, 4652.
28 I. Yanagi, R. Akahori, T. Hatano and K. Takeda, *Sci. Rep.*, 2014, **4**, 5000.
29 H. Kwok, K. Briggs and V. Tabard-Cossa, *PLoS One*, 2014, **9**, e92880.
30 I. Yanagi, T. Ishida, K. Fujisaki and K. Takeda, *Sci. Rep.*, 2015, **5**, 14656.
31 I. Yanagi and K. Takeda, *Nanotechnology*, 2021, **32**, 415301.
32 I. Yanagi, R. Akahori and K. Takeda, *Sci. Rep.*, 2019, **9**, 13143.
33 M. Wanunu, T. Dadosh, V. Ray, J. Jin, L. McReynolds and M. Drndić, *Nat. Nanotechnol.*, 2010, **5**, 807–814.
34 J. E. Hall, *J. Gen. Physiol.*, 1975, **66**, 531–532.
35 K. Venta, G. Shemer, M. Puster, J. A. Rodríguez-Manzo, A. Balan, J. K. Rosenstein, K. Shepard and M. Drndić, *ACS Nano*, 2013, **7**, 4629–4636.
36 Y. Goto, K. Matsui, I. Yanagi and K. Takeda, *Nanoscale*, 2019, **11**, 14426–14433.
37 E. Beamish, H. Kwok, V. Tabard-Cossa and M. Godin, *Nanotechnology*, 2012, **23**, 40530.
38 I. Yanagi, K. Fujisaki, H. Hamamura and K. Takeda, *J. Appl. Phys.*, 2017, **121**, 045301.
39 K. Matsui, I. Yanagi, Y. Goto and K. Takeda, *Sci. Rep.*, 2015, **5**, 17819.
40 K. Matsui, Y. Goto, I. Yanagi, Y. Yanagawa, Y. Ishige and K. Takeda, *Jpn. J. Appl. Phys.*, 2018, **57**, 046702.
41 S. W. Kowalczyk, A. Y. Grosberg, Y. Rabin and C. Dekker, *Nanotechnology*, 2011, **22**, 315101.
42 M. A. Alam, R. K. Smith, B. E. Weir and P. J. Silverman, in *IEDM Tech. Dig.*, 2002, pp. 151–154, DOI: 10.1109/IEDM.2002.1175801.
43 J. Sune and E. Y. Wu, *IEEE Electron Device Lett.*, 2003, **24**, 272–274.
44 S. Lombardo, C. Gerardi, C. Spinella, C. Bongiorno and A. La Magna, *J. Appl. Phys.*, 2005, **98**, 121301.
45 R. Degraeve, A. Kerber, G. Groeseneken and H. E. Maes, *IEEE Trans. Electron Devices*, 1998, **45**, 904–911.
46 K. Briggs, H. Kwok and V. Tabard-Cossa, *Nanotechnology*, 2015, **26**, 084004.
47 I. Yanagi, H. Hamamura, R. Akahori and K. Takeda, *Sci. Rep.*, 2018, **8**, 10129.